Review Article

Chunnan Hao, Zenan Ni*, Jian Wang, Huimin Liu*, Ze Zheng, Yuqiao Li, Jiawen Guo, Ruiqi Zhang, and Qijian Zhang*

A review of semiconductor photocatalyst characterization techniques

https://doi.org/10.1515/revac-2023-0061 received June 06, 2023; accepted September 15, 2023

Abstract: Photocatalysis is expected to solve both energy and environmental problems at the same time. Photocatalysis technology has received increasing attention, and systematically understanding the reaction mechanism of the photocatalytic process is very important for better utilization of solar energy. With the aim of establishing property-performance relationships and discovering the reaction mechanisms, several characterization techniques have been adopted to evaluate the properties of semiconductor photocatalysts, such as UV–visible absorption spectroscopy, photoluminescence spectroscopy, Raman spectroscopy, electrochemical impedance spectroscopy, and cyclic voltammetry. In this review, the principles and characteristics of different characterization techniques are demonstrated with concrete examples to give a clear picture and promote the research of photocatalysis in the future.

Keywords: photocatalysis, characterization techniques, semiconductor photocatalysts

1 Introduction

In order to cope with the continuous spread of energy shortage and environmental pollution, human beings have to focus on developing and utilizing sustainable energy [1]. Because of its inexhaustible and clean peculiarities, solar

* Corresponding author: Zenan Ni, School of Chemical and Environmental Engineering, Liaoning University of Technology, Jinzhou 121001, P. R. China, e-mail: hgnzn@lunt.edu.cn

Chunnan Hao, Jian Wang, Ze Zheng, Yuqiao Li, Jiawen Guo, Ruiqi Zhang: School of Chemical and Environmental Engineering, Liaoning University of Technology, Jinzhou 121001, P. R. China

energy has been considered the great potential to replace traditional fossil fuels [2,3].

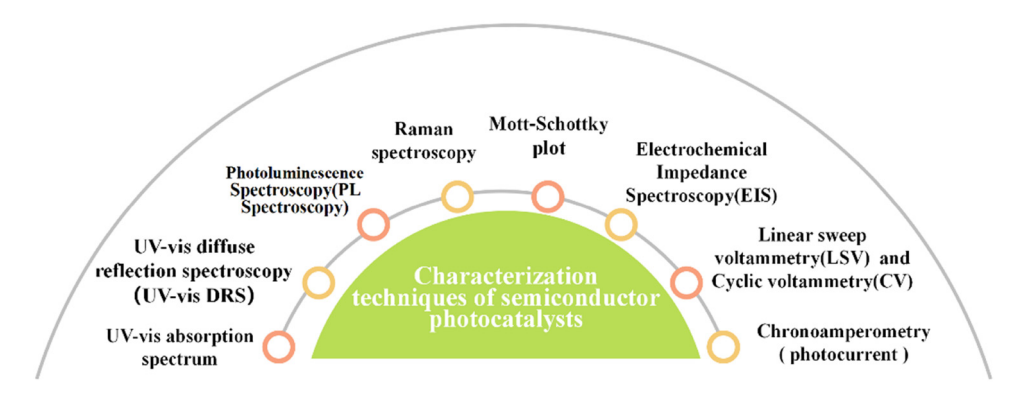
Photocatalysis is one of the most promising research directions in the utilization of solar energy [4,5], and sunlight could be used as the energy source to promote reactions. As a milestone discovery in the 1970s, Fujima and Honda introduced visible light into an electrochemical water-splitting system and revealed that the introduced light can promote the chemical reaction. It is worth mentioning that their work played a pioneering role and provided a powerful foundation for the research of other researchers in the following decades [6–8]. Since then, researchers on photocatalysis bloomed, and a lot of photocatalytic reactions such as water splitting, CO₂ reduction, decomposition of inorganic/organic pollutants, and synthesis of fine chemicals have been studied deeply [9–11].

Nevertheless, photocatalytic systems generally suffer from low light utilization efficiency because the mechanism of photocatalysis is not thoroughly studied. In order to improve the utilization of solar energy, a lot of work has been done to make clear the reaction mechanism [12,13]. As reported, the light absorption properties, structure, composition, charge transfer resistance, and separation efficiency of photogenerated electron-hole pairs could affect the reaction and these factors could be tested via optical properties [14-19]. Even though UV-visible (UV-vis) absorption spectroscopy was discovered more than 100 years ago, it was not commonly used due to the complicated operation as well as the lack of understanding of the principle [20]. Until 1995, the Kubelka-Munk equation was found to reflect the light absorption performance of photocatalysts and characterize the optical properties of photocatalysts. The formulation of the Kubelka-Munk equation has set up a strong link to the investigation and in-depth study of the optical properties of semiconductor photocatalysts [21]. After that, researchers can determine the type of semiconductor catalysts and the position of flat band potential by the Mott–Schottky plot [22]. In 2000, the photocurrent technique entered people's vision, and it is now widely used to test the transfer ability of photogenerated electrons [23]. In Scheme 1, the semiconductor photocatalyst characterization techniques are usually carried

^{*} Corresponding author: Huimin Liu, School of Chemical and Environmental Engineering, Liaoning University of Technology, Jinzhou 121001, P. R. China, e-mail: liuhuimin08@tsinghua.org.cn

^{*} Corresponding author: Qijian Zhang, School of Chemical and Environmental Engineering, Liaoning University of Technology, Jinzhou 121001, P. R. China, e-mail: zhangqijian@tsinghua.org.cn

2 — Chunnan Hao et al. DE GRUYTER



Scheme 1: Characterization techniques of semiconductor photocatalysts.

out including UV–vis absorption spectroscopy, photoluminescence spectroscopy (PL spectroscopy), Raman spectroscopy, electrochemical impedance spectroscopy (EIS), cyclic voltammetry (CV), and linear sweep voltammetry (LSV).

Zhang et al. [24] provide an overview of the current state-of-the-art preparation methods and characterization techniques for diatomic catalysts (DACs). The authors use the characterization techniques to determine the active center, the bond energy, electron transfer number, bond length, and other parameters of the diatoms at different adsorption sites; the most favorable adsorption sites can be determined by comparing them with the experimental data, which provides a theoretical basis for the preparation of new efficient and stable DACs. Besides, Ali et al. [25] summarized the relevant characterization techniques of iridium nanoparticle catalysts, such as transmission electron microscopy, scanning electron microscopy (SEM), X-ray diffraction, Fourier transform infrared spectroscopy, and other characterization techniques, to obtain the properties of the iridium catalysts such as the structures, phases, and functional groups, which can promote further development of the iridium catalysts. Luo et al. [26] focus on a review of advanced characterization techniques for the structure and photocatalytic properties of TiO2-based materials, leading to the design of novel photocatalysts with high solar energy conversion efficiency. Moreover, Janáky et al. [27] summarized the photoinduced interaction at the semiconductor interface and explored the specific surface area, carrier mobility, and charge transfer kinetics of the photocatalyst through some characterization. Zhang et al. [28] focus on evaluating the physical properties and chemical composition of semiconductor catalysts and the band structure through characterization techniques.

Therefore, in this article, the main characterization techniques of semiconductor photocatalysts are reviewed, and the principle and the use are elaborated in detail, which could help newcomers quickly understand the basic

principles and functions of these characterization techniques. In addition, for people can understand these characterization techniques more intuitively and systemically, various characterization techniques of semiconductor photocatalysts are supplemented by examples. Importantly, on the basis of summarizing the information obtained by various characterization techniques, the performance-performance relationship and reaction mechanism are revealed, so that researchers can regulate the most suitable reaction conditions and prepare excellent semiconductor photocatalysts. In conclusion, by summarizing the characterization technology and mechanism of photocatalysis, this article will effectively help scientific researchers explore the mechanism of semiconductor catalysts more deeply and also provide useful guidance for the development of photocatalysis technology and semiconductor.

2 Techniques for the characterization of properties of the semiconductor photocatalysts

2.1 UV-vis absorption spectroscopy

It is accepted that UV–vis absorption spectroscopy takes advantage of the electron transition in the photocatalyst under light irradiation [29,30]. Chromophores are the structural systems in which molecules can absorb ultraviolet or visible light. The type of electron transition varies with the structure of the chromophores [31,32]. Therefore, different chromophore structures in the photocatalysts lead to disparate types of electronic transitions [33–35]. Meanwhile, each material exhibits a unique and fixed absorption peak at a specific location in the UV–vis absorption spectra [21]. According to the

position and intensity of the absorption peak, the structure information of the semiconductor photocatalyst could be inferred [20].

UV-vis absorption spectroscopy could be used to characterize the ability of catalysts to harvest UV light and visible light [36]. For example, He et al. prepared the Cu/ZnO catalyst for photocatalytic CO2 hydrogenation, where pure Cu and ZnO were used as reference catalysts [37]. Cu and ZnO were studied on the UV-vis spectrophotometer (UV-2600, Shimadsu, Japan) equipped with a photometric integrating sphere. As can be seen from Figure 1(a), ZnO exhibits a strong absorption peak in the range from 200 to 500 nm, and the maximum absorption peak is 372 nm, indicating that ZnO can absorb UV light effectively, but cannot absorb visible light. The Cu/ZnO catalyst has two absorption peaks at 387.5 and 578.6 nm, corresponding to the absorption of ZnO and plasma Cu, respectively. The absorption peak area of Cu was obviously lower than that of Cu/ZnO. The larger absorption peak area means that more light was absorbed over the photocatalyst. Therefore, it proved that the structure information of photocatalysts can be calculated according to the position and intensity of the absorption peak. The results in Figure 1(a) indicated that the Cu/ZnO catalyst could absorb UV and visible light, and the strongest light absorption capacity was also illustrated. During photocatalytic CO₂ hydrogenation reaction under UV-vis light irradiation, the electrons excited by plasmonic Cu and semiconductor ZnO accelerated the pyrolysis of H₂ and the adsorption of CO₂, which promoted the catalytic reaction. As shown in Figure 1(b), the yield of CH₄ over the Cu/ZnO catalyst was significantly increased under light illumination.

UV-vis absorption spectroscopy could also be used to calculate semiconductor band gap width via the Tauc equation (also known as the Tauc Plot method, Eq. 1), which plays a practical role in measuring the conductivity of semiconductors [38].

$$(\alpha h \nu)^{1/n} = B(h \nu - E_g) \tag{1}$$

In Eq. 1, hv for the photon energy, α for the absorption index, h for Planck constant ($h \approx 4.13567 \times 10^{-15} \, \text{eV} \cdot \text{s}$), v for the frequency, B for the proportional constant, and E_g for the semiconductor band gap width. Exponent n is straightly connected with the type of semiconductor, n = 1/2 for direct bandgap semiconductor, while n = 2 for indirect bandgap semiconductor.

Specific operation of this method is shown as follows. First, $(\alpha h v)^{1/n}$ and h v are calculated. c means the speed of light ($c = 3.0 \times 108 \,\mathrm{m\cdot s^{-1}}$) and λ means the wavelength of light in the formula of $v = c/\lambda$. In general, $\alpha = 2.303 \times A/d$, where A is the absorbance, which can be measured by spectrophotometer. For liquid, d is the thickness of the colorimeter; for solid, d is the thickness of the film; and for powder, d is the thickness of the powder tablet. Then, we can plot $(ahv)^{1/n}$ with respect to hv (hv is the x-coordinate, $(\alpha h \nu)^{1/n}$ is the y-coordinate), and a curve approximating a straight line is obtained. After that, the straight-line part of the graph is extrapolated to the x-axis, where the intersection is the band gap value. There is another easy way to calculate the band gap width of semiconductors [39,40]. The fundamental theory is that the band edge wavelength of semiconductor (also named absorption threshold, λ_g) is determined by the band gap width $E_{\rm g}$. The Eq. 2 shows the quantitative connection of above two parameters.

$$E_{\rm g}({\rm eV}) = h\nu = h/k \times c/\lambda = [6.63 \times 10^{-34} \, {\rm J \cdot s}]/[1.6 \times 10^{-19} \, {\rm J \cdot eV^{-1}}] \times [3 \times 10^{17} \, {\rm nm \cdot s^{-1}}]/$$
 (2)
 $\lambda = 1{,}240/\lambda_{\rm g}({\rm nm})$

On the curve of the absorption spectrum, a tangent line is made along the point where the curve changed the most, and the intersection of the tangent line and X-axis is recorded as $\lambda_{\text{g}}\text{,}$ and then Eq. 2 is used to calculate the band gap $E_{\rm g}$.

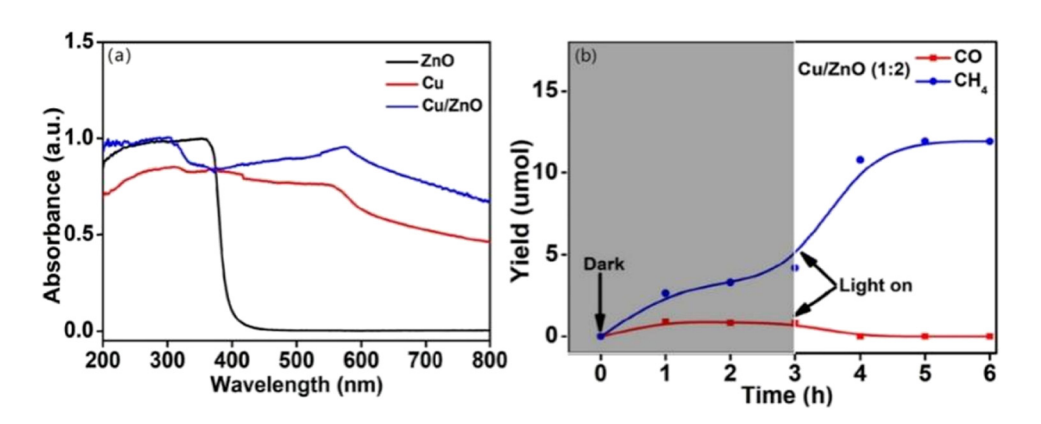


Figure 1: (a) UV-vis absorption spectra of the prepared catalysts; (b) yields of CH₄ and CO over Cu/ZnO catalyst in photocatalytic CO₂ hydrogenation reaction [37].

A typical example for the calculation of band gap width from UV-vis absorption spectrum was provided by Nor and Amin's study [41]. The C-doped TiO₂ photocatalysts with different C content were prepared for CO2 reduction reaction, and Eq. 1 was used to calculate the band gap. As shown in Figure 2(a), the band gap of TiO₂ and 6C-TiO₂ were obtained (TiO2 and 6C-TiO2 are direct band gap semiconductors, so n is equal to 1/2). Apparently, the band gap of 6C-TiO₂ was narrowed from 3.37 to 3.10 eV (inset of Figure 2(a)). The narrow band gap of 6C-TiO₂ is conducive to the movement of photogenerated electrons, and the electron-hole has a high possibility of absorbing visible light. In addition, the narrow band gap of 6C-TiO₂ helped to absorb visible light, generating a huge visible light response in the reaction process. As can be seen from Figure 2(b), compared with pure TiO2, the yield of the target product methanol was almost doubled over the 6C-TiO2 catalyst.

2.2 UV-vis diffuse reflection spectroscopy (UV-vis DRS)

UV—vis DRS can be used to characterize the light reflection ability of a small number of powder photocatalysts [42,43]. Similar to UV—vis absorption spectroscopy, UV—vis DRS also utilizes the electron transition of photocatalysts upon light irradiation. It mainly takes advantage of the reflection of light on the surface of a substance to obtain the information of the semiconductor photocatalysts, which is closely related to its electronic structure. In addition, compared with the UV—vis absorption spectrum, the UV—vis DRS spectrum of the measured solution sample state is required. These solution samples cannot be clarified, but rather suspension or emulsion [44—46].

Light would be reflected and scattered when it strikes a solid surface. If the light causes specular reflection, the magnitude of the angle of reflection is the same as the magnitude of the angle of incidence. When light strikes the surface of a powdered particle, some light is reflected onto the surface of each particle [47,48] and other light is refracted inside the surface particles. After part of absorption, the radiation would transfer to the internal grain interface and then reflected, refracted and absorbed. It is repeated many times and eventually reflected from the powder surface in all directions, which is called diffuse light. In addition, when the diffuse light passes through a solid powder, if absorbed by the powder, the diffused light is weakened, and there is a relationship between the wavelength and intensity of the diffused light, resulting in a diffuse spectrum [49–51].

UV-vis DRS depends on the physicochemical properties and color of the semiconductor photocatalyst surface, so characterizing the optical properties of the semiconductor photocatalyst is very useful. The Kubelka–Munk equation (also known as the law of diffuse reflection, Eq. 3) is commonly used to describe the optical relationship on a solid that can both absorb and reflect light [52,53].

$$F(R_{\infty}) = \frac{K}{S} = \frac{(1 - R_{\infty})^2}{2R_{\infty}}$$
 (3)

Here, K is for the absorption coefficient, S for the scattering coefficient, R_{∞} for the reflectivity of an infinitely thick sample, and $F(R_{\infty})$ for the reductive of Kubelka–Munk function.

Pascariu gave a representative example for the characterization of optical properties of photocatalysts via UV-vis DRS [54]. TiO_2 and Cu/TiO_2 nanocomposites (T400, TCu1, TCu2, TCu3, TCu4, and TCu5 were used to represent the catalysts with Cu/TiO_2 ratios of 0, 0.05, 0.1, 0.5, 1, and 2,

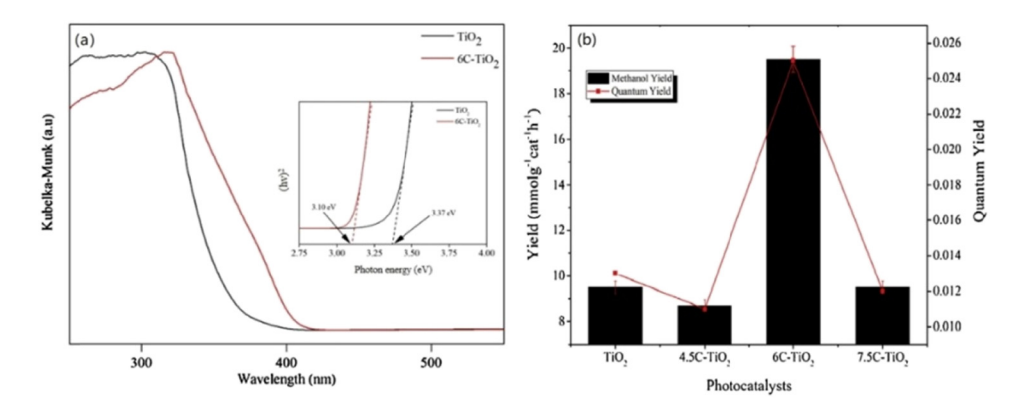


Figure 2: (a) UV–vis absorption spectra of TiO_2 and $6C-TiO_2$, with the inset displaying the Tauc plot for band gap recognition of TiO_2 and $6C-TiO_2$; (b) yield and quantum yield of methanol over the catalysts [41].

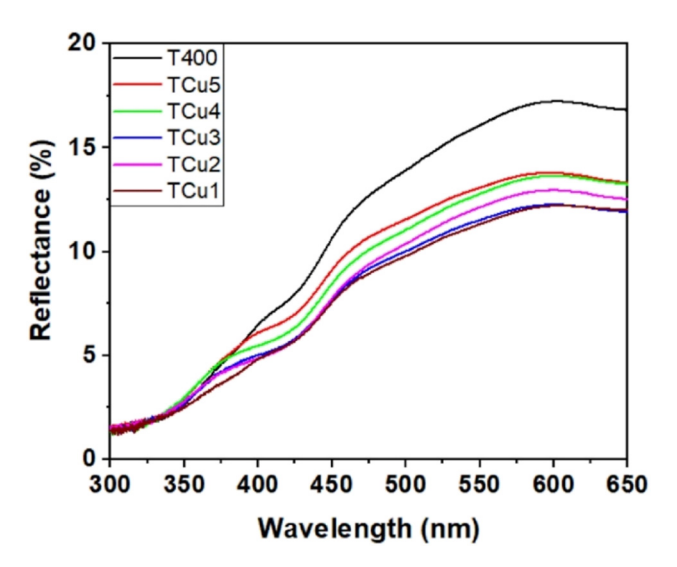


Figure 3: UV-vis DRS spectra of TiO₂ (T400) and Cu/TiO₂ photocatalysts [54].

respectively) by electrostatic spinning calcination method. From Figure 3, the photocatalyst without Cu doping (T400) reflected more light than other catalysts and TCu1 exhibited the least reflectance. It could be assumed that TCu1 possessed better light absorption capacity than other catalysts. The better light harvesting capacity of TCu1 made it the best catalyst for the removal of amaranth dye from synthetic wastewater, with a degradation efficiency of 99.84%. In addition, the band gap width can be calculated by Eqs. 1 and 3.

In order to give a better understanding of the usage of UV-vis absorption spectrum and UV-vis DRS in the field of photocatalysis, several examples in the last 3 years (as shown in Table 1) are added. It is generally accepted that a lower band gap could improve degradation efficiency.

2.3 PL spectroscopy

When the semiconductor is excited by light with a photon energy greater than or equal to its band gap E_g , electrons

would be photoexcited and leave holes in the valence band (VB) in the process of conveying from VB to conduction band (CB). For semiconductor photocatalysts, their thickness is small, so the absorption of photogenerated electrons and holes by themselves is negligible. At the same time, the electrons and holes generated in CB and VB on semiconductor photocatalytic materials are still in noneguilibrium state, and they will reach an equilibrium state (quasi-equilibrium state) after a period of diffusion and further recombination [58]. Partial of the electrons and holes could be directly or indirectly captured by the defect levels and holes, while some of the quasi-equilibrium electrons and holes could recombine, and some electrons may return from the excited state to the ground state under photoexcitation. The captured, recombined, or returned electrons and holes would emit light at different frequencies and form the PL spectrum [59]. PL Spectroscopy is an important method to evaluate the recombination of electrons and holes of semiconductor photocatalysts. Generally, higher PL strength will lead to a higher photoelectron-hole pair recombination rate, which is not conducive to electron transition in photocatalytic reactions [60]. Moreover, PL spectroscopy could also provide significant information on the optical and photochemical properties, electronic structure, and the potential defects in the interfacial region of semiconductor photocatalysts [61].

Kumari et al. gave a representative demonstration of the application of PL spectroscopy to describe the optical properties of photocatalysts [62]. The h-BN-MoS₂ heterostructures (MoS₂ was uniformly distributed on hexagonal boron nitride (h-BN) nanosheets) were prepared by hydrothermal method, and MoS₂ as well as h-BN were used as references. According to Figure 4(a), h-BN and MoS₂ exhibited wide emission bands in the wavelength ranges of 435–560 and 460–580 nm, respectively. h-BN-MoS₂ gave the PL spectrum within the narrowest wavelength range. Most importantly, the PL intensity of h-BN-MoS₂ was observably lower than those of the reference catalysts, proving the better photoelectron-hole pair separation and photoelectron transfer capacity. In other words, the higher the

Table 1: Examples of applications of UV-vis absorption spectroscopy or UV-vis DRS

Catalyst	Absorption peak range	Synthesis method	Band gap of catalysts	Degradation efficiency (%)	Ref.
rGO/ZnO	274 and 376 nm	Ecofriendly hydrothermal method	ZnO: 3.06 eV rGO/ZnO: 2.35 eV	97	[55]
$Zn-TiO_2$ $MnMoO_4$ / $NiFe_2O_4$	400–700 nm 400–800 nm	Sol–gel method Coprecipitation and hydrothermal routes	TiO ₂ : 3.0 eV Zn-TiO ₂ : 2.8 eV NiFe ₂ O ₄ : 1.20 eV MnMoO ₄ / NiFe ₂ O ₄ : 1.06 eV	99.64 96	[56] [57]

6 — Chunnan Hao et al. DE GRUYTER

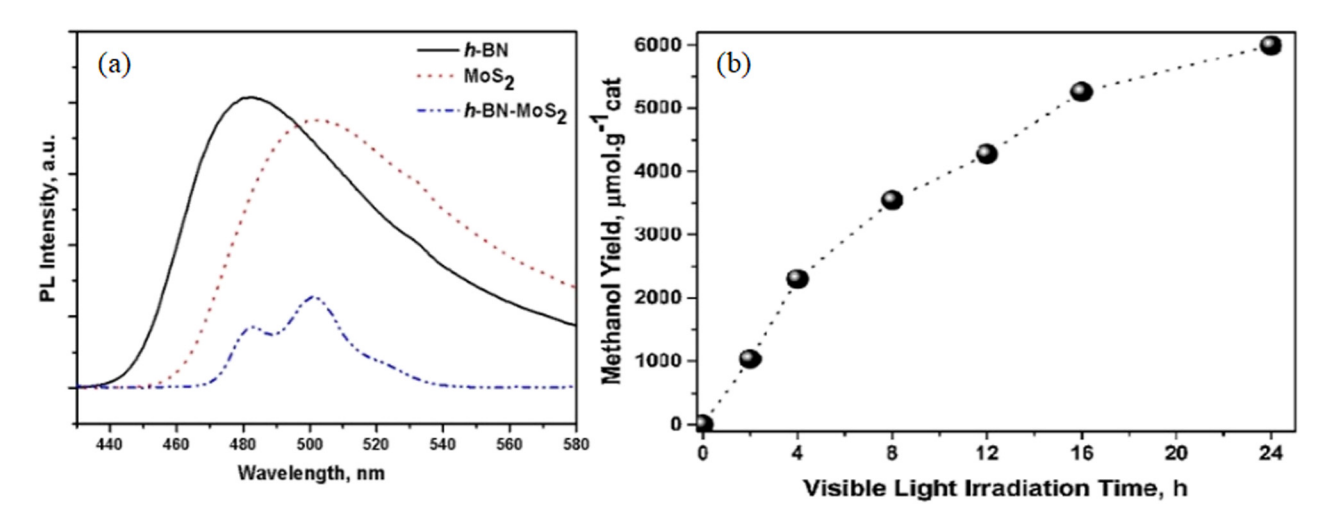


Figure 4: (a) PL Spectra of prepared catalysts. (b) Change of methanol yield over h-BN-MoS₂ with visible light irradiation time [62].

PL intensity, the higher the recombination rate of photoelectron hole pairs. The highly efficient photoelectron—hole pair separation and photoelectron transfer capacity of h-BN-MoS₂, together with its strong light-harvesting capacity, endowed it with the best catalytic performance in photocatalytic CO_2 reduction into CH_3OH , with the maximum yield toward methanol of 5,994 μ mol·g⁻¹ (Figure 4(b)).

To further illustrate the application of PL spectroscopy in the characterization of semiconductor photocatalysts, several examples from the past 3 years have been supplemented (as shown in Table 2). The performance of the examples can also be seen: the lower the PL intensity, the lower the recombination rate of photoelectron-hole pairs, and the stronger the capability of the photocatalysts.

2.4 Raman spectroscopy

Raman effect was reported by Raman in 1928 [65,66]. When the material (gas, liquid, or transparent substance) is illuminated by monochromatic light whose wavelength is much shorter than the common size of sample, a large part of the light will be transferred along the direction of the incident light, while a small number of the light will be scattered at other angles to produce scattered light [67].

In the vertical direction, there are not only scattered light owning the same frequency with the incident light, but also a variety of symmetrically distributed extremely weak Raman spectrum lines offset with the incident light frequency. Generally, the frequency of the variable scattering rays is lower than that of the incoming rays. Occasionally, the frequency of the scattering rays is higher than that of the incoming rays, while the intensity is weaker. Moreover, the quantity, the displacement, and the length of Raman lines are

directly connected with the vibrational or rotational energy level of the molecular structure of the material [68–70]. The message of the vibration and rotation of molecules could be obtained from the scattering spectrum with different frequencies from the incident light [71,72].

Raman spectroscopy is often used to determine the structure and electronic properties of solid semiconductor photocatalysts. For a given semiconductor photocatalytic material (doped semiconductor photocatalytic material, semiconductor alloy photocatalyst, etc.), the effect of light, namely the light wave vibration and optical phonon displacement caused by light incident on semiconductor photocatalyst, could be explained by Raman spectroscopy. The general structural information of a given photocatalyst can be obtained by a variety of Raman spectral lines. The displacement of optical phonons also reflects the amount of photogenerated charge carriers generated by the doping of semiconductor photocatalysts. For example, Raman spectroscopy can be used to determine whether heterojunction structures are formed between the two components to further understand the performance of the photocatalyst [73–75].

An effective help for understanding the properties of photocatalysts via Raman spectroscopy was provided by Hamad et al. [76]. The $CuO@TiO_2$ heterojunction nanocomposite catalyst was prepared, and the Raman spectra of $CuO@TiO_2$ as well as the reference catalysts TiO_2 and CuO are shown in Figure 5. According to the Raman spectrum, the double E_g modes at 145 and 606 cm⁻¹ were corresponding to the symmetric vibration of O–Ti–O, and the B_{1g} mode at 437 cm⁻¹ was related to the symmetric bending vibration of O–Ti–O. The A_{1g} peak of CuO was located at 272 cm⁻¹ which was distinctive for analyzing the CuO phase. In $CuO@TiO_2$, the positions of Raman peaks of B_{1g} and A_{1g} vibration modes of TiO_2 were modified by CuO. In

Catalyst	Synthesis method	PL intensity	Photoelectron-hole pairs recombination rate	Photocatalytic capability	Ref.
MnMoO4, NiFe ₂ O ₄ , MnMoO./NiFe ₂ O.	Coprecipitation and hydrothermal routes	$NiFe_2O_4 > MnMoO_4 > MnMoO_4/NiFe_2O_4$	$NiFe_2O_4 > MnMoO_4 > MnMoO_4/$ $NiFe_2O_4$	$NiFe_2O_4 < MnMoO_4 < MnMoO_4/$ [57]	[57]
MnS, MnS@Ag ₂ S	Microwaveassisted solvothermal and ion-	$MnS > MnS@Ag_2S$	MnS > MnS@Ag ₂ S	MnS < MnS@Ag ₂ S	[63]
BiOCI, 10% Ag ₂ WO ₄ /BiOCl	excnange approacn A facile Coprecipitation method	BiOCl > 10% Ag₂WO₄/BiOCl	BiOCl > 10% Ag ₂ WO₄/BiOCl	BiOCl < $10\% \text{ Ag}_2\text{WO}_4/\text{BiOCl}$	[64]

addition, there was a blue shift for the B1g mode from 437 to 404 cm⁻¹, which indicated a strong interaction between CuO and TiO2 in CuO@TiO2. At the same time, it was also proved that heterostructure was formed between CuO and TiO₂. As reported, the heterojunction structure of CuO@TiO₂ endowed it with high catalytic activity in the photocatalytic degradation of organic pollutants.

Several examples from the last 3 years (shown in Table 3) are used as references. Raman spectroscopy can be used to determine whether a heterostructure is formed between two substances.

2.5 Mott-Schottky plot

Photocatalyst is usually a composite material of semiconductor or single component semiconductor. The type of semiconductors, the position of the CB, the position of the VB, and the width of the bandgap influence the performance of photocatalysts efficiently [79]. Hence, it is of great significance to investigate these properties of semiconductor photocatalysts. UV-vis absorption spectrum, mentioned above, is powerful for characterizing the bandgap width of the semiconductors, and Mott-Schottky plot is a characterization technique that is broadly used to determine the type of semiconductors and band potentials [27,80].

$$\frac{\mathrm{d}^2\Phi}{\mathrm{d}x^2} = -\frac{\rho}{\varepsilon\varepsilon_0} \tag{4}$$

Mott-Schottky equation derivation starts from the Poisson equation (as shown in Eq. 4), which expresses

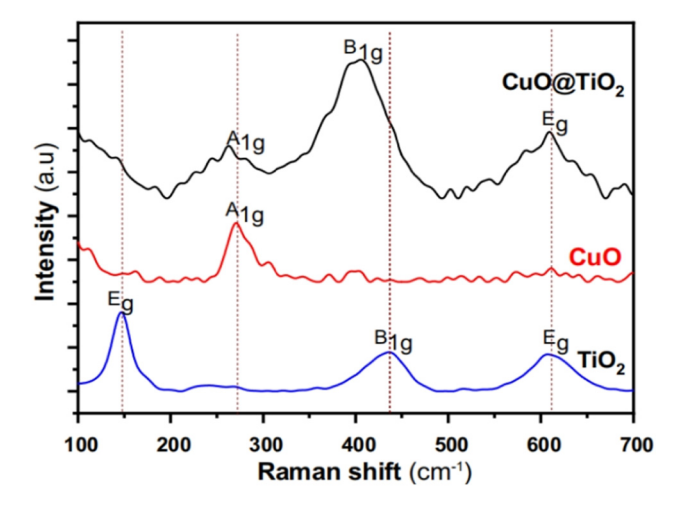


Figure 5: Raman spectra of TiO₂, CuO, and its binary CuO@TiO₂ heterojunction nanocomposite catalyst [76].

8 — Chunnan Hao et al. DE GRUYTER

Table 3: Examples of applications of Raman spectroscopy

Catalyst	Synthesis method	Positions of Raman peaks (cm ⁻¹)	The corresponding structure	Ref.
rGO/ZnO	Ecofriendly hydrothermal method	438	438 cm ⁻¹ : ZnO	[55]
		1,351	1,351 cm ⁻¹ : D band	
		1,586	1,586 cm ⁻¹ : G band	
GO/Ag ₂ O	Modified Hummers method	112.97	112.97 cm ⁻¹ : Ag–O bond	[77]
_		1,350	1,350 cm ⁻¹ : D band	
		1,587	1,587 cm ⁻¹ : G band	
CuO/CdS	The ultrasound-assisted wet impregnation method	216	216, 413, 601 cm ⁻¹ : CdS	[78]
		283		
		332		
		413	283, 332, 627 cm ⁻¹ : CuO	
		601		
		627		

the connection with charge density and potential difference Φ , where the position x away from the semiconductor surface's charge density is ρ , Φ is the potential difference, ε is the dielectric constant, and ε_0 is the vacuum dielectric constant. Boltzmann distribution is used to explain the distribution of electrons in the space charge region, and Gauss' law between the electric field passing through the interface and the charge contained in the region. Poisson equation can be solved, and Mott–Schottky equation can be obtained [81].

$$\frac{1}{C_{\rm SC}^2} = \frac{2}{\varepsilon \varepsilon_0 e N_{\rm d}} \left(U - U_{\rm FB} - \frac{k_{\rm B} T}{e} \right) \tag{5}$$

Eq. 5 is the Mott–Schottky equation, which expresses the connection between the space charge layer differential capacitance ($C_{\rm sc}$) of a semiconductor and other parameters [82], where U is the applied potential, ε is the dielectric constant, ε_0 is the vacuum dielectric constant, e is the electron charge, $k_{\rm B}$ is the Boltzmann constant, and T is the absolute temperature.

On account of the data in the formula, a graph could be obtained, with U as the x-coordinate and $C_{\rm SC}^{-2}$ as the y-coordinate. The graph usually shows an upward curve, which is close to a straight line, and a tangent line down along the curve could be made. The tangent line intersects the x-axis and the resulting intercept is the flat-band potential $U_{\rm FB}$. For n-type semiconductors, their flat band potential and CB are considered to be nearly identical, so the obtained flat band potential can be directly described as $E_{\rm CB}$ [83]. In addition, doping density $N_{\rm d}$ is the slope of this tangent line. The slope can be used to determine the type of semiconductors. The n-type semiconductor and p-type semiconductor respectively have a positive slope and a negative slope [84,85].

$$E_{\rm g} = E_{\rm VB} - E_{\rm CB} \tag{6}$$

It is worth noting that, by combining the bandgap width $E_{\rm g}$ measured by UV–vis absorption spectroscopy, the position of VB could be calculated via Eq. 6. The type of semiconductors, the width of bandgap, as well as the positions of VB and CB play crucial roles in photocatalytic reaction, as they directly affect the photocatalytic reaction process [86].

Yadav's work is a representative pattern of using Mott-Schottky plots to determine the flat band potential of photocatalysts [87]. They synthesized a catalyst with Pt nanoparticles incorporated by Si sites on mesoporous Tix- $Si_{1-x}O_2$ support (the catalyst was denoted as PtSi- $Ti_{0.72}Si_{0.28}O_2$ in the case that x = 0.72), where Pt-TiO₂ and Pt-Ti_{0.72}Si_{0.28}O₂ were adopted as reference catalysts. The tangent lines of the Mott-Schottky curves of the three semiconductor photocatalysts in Figure 6 showed that the slopes of the three tangent lines are all positive, which indicate that the three catalysts are n-type semiconductors. In addition, they utilized Eq. 5 to determine the flat-band potential, which is obtained by making a tangent to the curve in Figure 6. Pt-TiO₂, Pt-Ti_{0.72}Si_{0.28}O₂, and Pt_{Si}-Ti_{0.72}Si_{0.28}O₂ catalysts' flat-band potentials, which were directly described as E_{CB} , were -0.30, -0.54 and -0.40 eV. The relative negative potential (-0.40 eV) of CB of Pt_{Si}-Ti_{0.72}Si_{0.28}O₂ relative to the potential of CO₂ for CO, CH₄, and CH₃OH and its strong light response endow Pt_{Si}-Ti_{0.72}Si_{0.28}O₂ with higher photocatalytic activity for CO, CH₄, and CH₃OH reduction by CO₂.

The position of VB is an important factor to determine whether a semiconductor can reasonably carry out the oxidation-half reaction, since the position of VB should be more positive than the redox potential of the reactants.

An example to illustrate how to solve VB through Mott–Schottky plots and UV–vis absorption spectroscopy was shown by the study of Zhu et al. [88]. Typically, ZnO and CeO₂ photocatalysts were prepared, and Eq. 5 was used

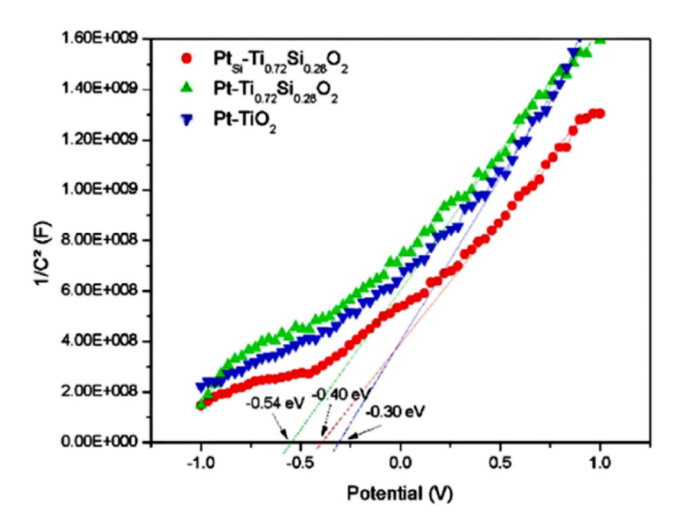


Figure 6: Mott-Schottky plots of Pt-TiO₂, Pt-Ti_{0.72}Si_{0.28}O₂, and Pt_{Si}-Ti_{0.72}Si_{0.28}O₂ [87].

to determine the flat-band potentials, which were obtained by targeting the curve in Figure 7(a). The flat band potentials of ZnO and CeO₂ were -0.61 and -0.87 eV, respectively. It was clear that both photocatalysts were n-type semiconductors. The flat band potential is nearly equivalent to $E_{\rm CB}$ as far as know. Therefore, the $E_{\rm CB}$ of ZnO and CeO₂ were -0.61 and -0.87 eV, respectively. And the relatively negative position of CB of CeO₂ and ZnO was more negative than that of O₂ reduced to 'O²⁻ radical. Then, they obtained the Eg of CeO2 and ZnO using UV-vis absorption spectroscopy in Figure 7(b) and Tauc equation (Eq. 1), and the $E_{\rm g}$ of ZnO and CeO₂ which is shown in Figure 7(c) were 3.13 and 2.86 eV, respectively. According to Eq. 6, E_{VB} of ZnO and CeO₂ could be calculated as 2.52 and 1.99 eV, separately. The redox potential of water oxidation to 'OH radical is 2.24 eV. Therefore, OH radical could be generated at the VB position of ZnO; at the same time, it could not be generated at the VB position of CeO₂. However, due to the fast recombination of photoinduced electron-hole pairs on ZnO, the photocatalytic

activity of ZnO was poor. ZnO/CeO_2 Z-scheme heterostructure with CB more negative than CeO_2 and VB more positive than ZnO exhibited stronger reduction and oxidation ability. As a result, the optimal ZnO/CeO_2 Z-scheme heterostructure (denoted as ZnO/CeO_2 -3, in which the mass fraction of CeO_2 was 30%) performed better photostability and higher efficiency for the photodegradation of RhB, which was 2.5 times and 1.7 times of pure ZnO and CeO_2 .

2.6 EIS

EIS, also known as alternating current (AC) impedance, is currently used to understand the charge transfer situation in photoelectrochemical catalytic reactions. It is also one of the widely used characterization methods for photocatalysts and is very intuitive and effective [89,90]. The electrochemistry involved in photocatalysis is relatively complex. Hence, electrochemical systems can be considered simply as equivalent circuits and studied, and the essential components (such as inductors (L), capacitors (C), and resistors (R)) are connected in series or parallel. The structure of the equivalent circuit and the information of each element can be specified via EIS, and the composition of the electrochemical system as well as the properties of the electrode can be analyzed by the electrochemical significance of these elements [91,92].

EIS measures the variation of the ratio of AC potential to current signal with the change of sinusoidal frequency ω , applying small amplitude AC sinusoidal potential waves of distinct frequencies. In other words, the phase angle of impedance varies with ω by applying small amplitude AC sinusoidal potential waves of different frequencies [93]. It is equivalents to entering a disturbance function X in an electrochemical workstation, and it will output a response signal Y. It forms a function that describes the effect of the

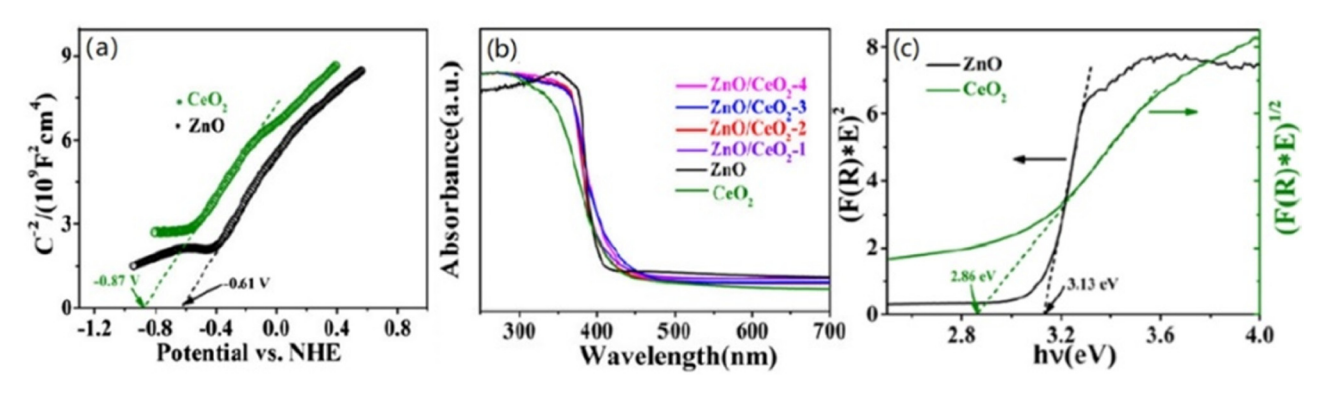


Figure 7: (a) Mott-Schottky plots, (b) UV-vis absorption spectra, and (c) band gap energies of different catalysts [88].

disturbance on the response, and it is named the transfer function $G(\omega)$. If the internal structure of the system is a stable linear structure, there is a linear function relationship between the output signal and the disturbance signal [94]. It could be expressed by Eq. 7:

$$Y = G(\omega)X \tag{7}$$

- (1) If the angular frequency is ω , X is its sinusoidal current signal, and then, Y is its sinusoidal potential signal. In cases like that, the transmission function $G(\omega)$ is also a frequency function, which is called the frequency response function. The function of this frequency response is called the impedance of the system, and it is represented by Z.
- (2) If the angular frequency is ω , X is its sinusoidal potential signal, and Y is its sinusoidal current signal. In cases like that, the frequency response function $G(\omega)$ is called the admission of the system and is expressed by Y.
- (3) Impedance and admittance are collectively referred to as resistance, and they are denoted by G. Impedance and admittance are reciprocal: Z = 1/Y.
- (4) Resistive G is a vector that varies with ω , and it is usually expressed as a complex function of angular frequency ω . There is a quantitative relationship between the parameters (Eq. 8). Here, G' is the real section of the resistance and G' is the imaginary component of the resistance, and j is an imaginary unit, $j = \sqrt{-1}$. And it can be simplified as Eq. 9. The modulus value of impedance is displayed in Eq. 10. In addition, the phase angle φ of impedance is shown in Eq. 11.

$$G(\omega) = G'(\omega) + jG''(\omega)$$
 (8)

$$Z = Z' + iZ''^2 \tag{9}$$

$$|Z| = Z' + Z'' \tag{10}$$

$$\tan \varphi = \frac{-Z''}{Z'} \tag{11}$$

From the Eqs. 7–11, we can get different frequencies of impedance real section Z, imaginary component Z, modulus value |Z|, and phase angle φ . Finally, the real part Z and the imaginary part Z are taken as X-axis and Y-axis, respectively, to form the EIS spectrum. In the characterization of semiconductor photocatalysts, the obtained EIS spectrum usually looks like a semicircle curve [95]. In general, we can know the charge transferability of the catalyst according to the radius of the arc in the EIS spectrum of the catalyst. The larger the arc radius, the larger the charge transfer resistance and the weaker the charge transfer capability [27].

A typical example of adopting the EIS spectrum to characterize photocatalysts was provided by Wu [96]. TiO₂ and Cu-TiO₂ catalysts were produced by the sol-gel method, and a series of NCT catalysts by further impregnating different amounts of Ni onto Cu-TiO2. The EIS spectra in Figure 8(a) revealed that the arc radius of NCT catalysts was smaller than those of other catalysts. Among them, the radius lengths of 0.5 NCT and 1.0 NCT arcs were the smallest. It could be assumed that 0.5 NCT and 1.0 NCT possessed a smaller charge transfer resistance than other catalysts and accelerated charge transfer capacity. Together with the weaker photoelectron-hole pair recombination rate characterized via PL spectra in Figure 8(b), 0.5 NCT exhibited good catalytic performance in photocatalytic H₂O reduction to H₂, with its catalytic yield almost 40 times higher than that of bare TiO₂ (Figure 8(c)).

Several examples of EIS in the field of photocatalysis in the last 3 years (as shown in Table 4) can fully demonstrate its importance. The data in Table 4 are also consistent with

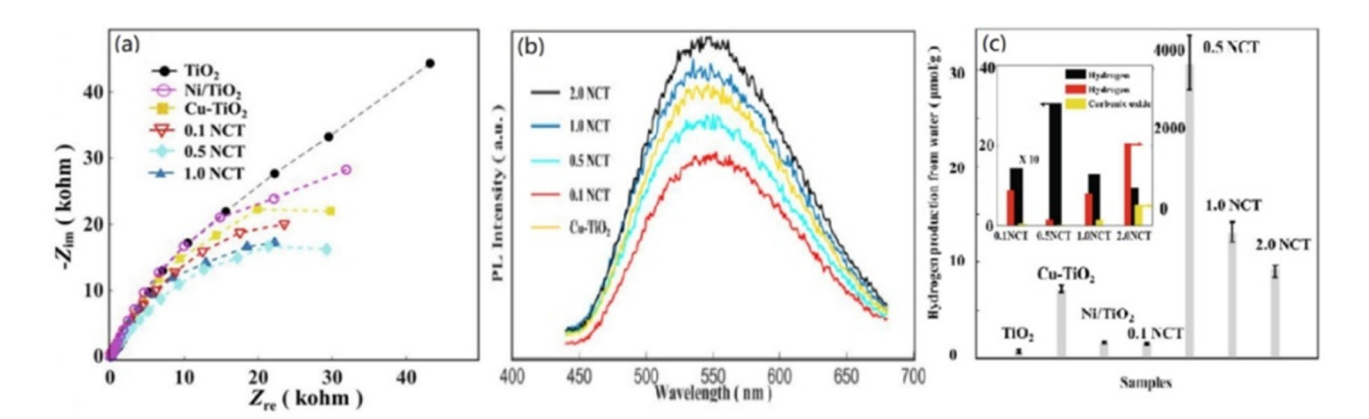


Figure 8: (a) The EIS of modified TiO₂ catalysts; (b) PL emission spectrum of NCT samples; (c) hydrogen yield from pure water on different catalysts [96].

Table 4: Examples of applications of EIS

Catalyst	Synthesis method	Arc radius	Charge transfer resistance	harge transfer resistance Charge transfer capability Photocatalytic capability Ref.	Photocatalytic capability	Ref.
CuO CuO/CdS	The ultrasound-assisted wet impregnation method	ethod CuO > CuO/CdS	CuO > CuO/CdS	CuO < CuO/CdS	CuO < CuO/CdS	[78]
BiOBr-H ₂ O BiOBr-EG	3iOBr–H ₂ O BiOBr–EG One-step hydrolysis method	$BiOBr-H_2O > BiOBr-EG$	BiOBr-H ₂ O > BiOBr-EG BiOBr-H ₂ O > BiOBr-EG	$BiOBr-H_2O < BiOBr-EG$	$BiOBr-H_2O < BiOBr-EG$	[67]
CdS 6% MoS ₂ /CdS	Simple sonication method	$CdS > 6\% MoS_2/CdS$	$CdS > 6\% MoS_2/CdS$	$CdS < 6\% MoS_2/CdS$	$CdS < 6\% MoS_2/CdS$	[86]

the above conclusion (the smaller the arc radius, the stronger the photocatalytic capacity).

2.7 LSV and CV

LSV is a standard photocatalytic characterization method. It applies a voltage that changes in a linear relationship on the electrode and records the electrolytic current on the working electrode [99]. If there is electron transfer (redox reaction), the current will increase. Meanwhile, the position of the current peak reflects diverse redox reactions, and the intensity of the current peak reflects the activity of redox reactions [100–102]. LSV is often used for quantitative analysis, and it is suitable for the determination of adsorbable substances. CV has the same working principle as LSV, but it is a cyclic process. Therefore, it is often used to judge the reversible electrode process as well as study the active substance in the electrode adsorption—desorption process [103–105].

The potential at any time after the start of scanning *E* can be expressed by Eq. 12 [106]:

$$E = E_i - vt \tag{12}$$

where E_i is the initial potential, t is the time, and v is the voltage scanning speed. The peak current of the reversible electrode reaction is shown in Eq. 13:

$$i_{\rm p} = \frac{0.4463F^{3/2}An^{3/2}D^{1/2}C_0v^{1/2}}{R^{1/2}T^{1/2}}$$
 (13)

where F is Faraday constant, D is the reactant diffusion coefficient, C_0 is the reactant concentration in oxidation state, n is the electron exchange number, and A is the effective electrode area. When the effective area of the electrode remains unchanged, Eq. 13 can be simplified into the following form:

$$i_{\rm p} = k v^{1/2} C_0$$
 (14)

It can be seen from Eq. 14 that the peak current is proportional to the 1/2 power of the potential scanning velocity ν , and the peak current is proportional to the bulk concentration of the reactants, which is the basis of the quantitative analysis of the linear scanning voltammetry.

However, if the reaction process of the electrode is irreversible, the peak potential will shift in the positive or negative with the increase of the scanning speed [107–109]. There is a quantitative relationship between the parameters (Eq. 15).

$$E_{\rm p} = E_{1/2} \pm 1.1RT/nF$$
 (15)

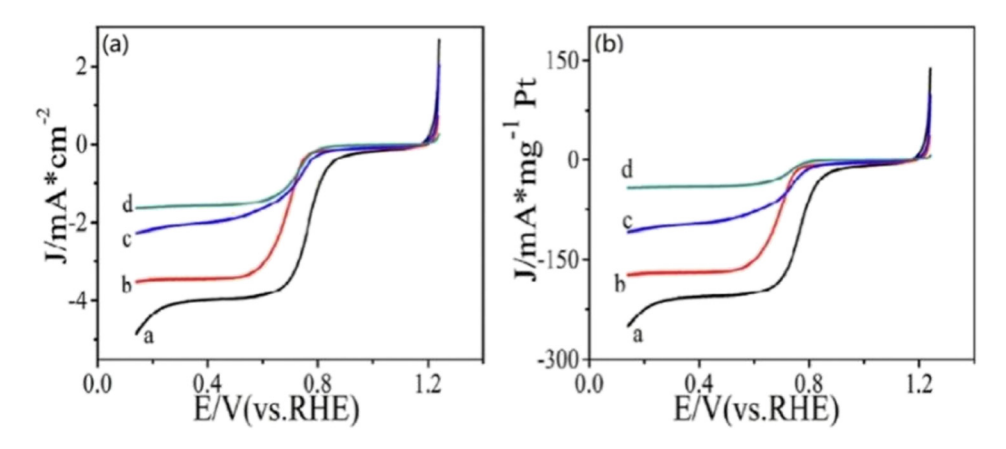


Figure 9: LSV Curves in oxygen-saturated H₂SO₄: a. Pt-WO₃@W/GNs, b. 30% PtRu/C, c. Pt/WO₃-GNs, d. Pt/GNs. (a) the specific activity and (b) mass activity given as current normalized against electrode surface area and the mass of Pt [110].

Li et al.'s work gives a representative example of the characterization of optical properties of photocatalysts via LSV and CV [110]. Pt/GNs, Pt/WO₃-GNs, and Pt-WO₃@W/GNs were prepared by the solid phase approach, with 30% PtRu/C as a reference catalyst. The four catalysts were used for electrocatalytic oxygen reduction reaction (ORR), with or without the illumination of a 0.25 mW·cm⁻² Xenon lamp. From Figure 9(a) and (b), it is suggested that the onset potential of Pt-WO₃@W/GNs was higher than those of other photocatalysts. The half-wave potentials of Pt-WO₃@W/GNs were higher than those of other photocatalysts. Since initial

potential and half-wave potential are the most important performance indexes of the catalysts used for electrocatalytic ORR, it can be speculated that Pt-WO₃@W/GNs exhibited better catalytic activity in ORR than the other three photocatalysts. In other words, the current peak mentioned earlier reflected the activity of the reaction. The initial potential and half-wave potential of Pt-WO₃@W/GNs were the largest, which expresses that Pt-WO₃@W/GNs have the highest catalytic activity. In Figure 10, the mass activities of the four catalysts for electrocatalytic ORR with or without light radiation were demonstrated. As shown in Figure 10(a),

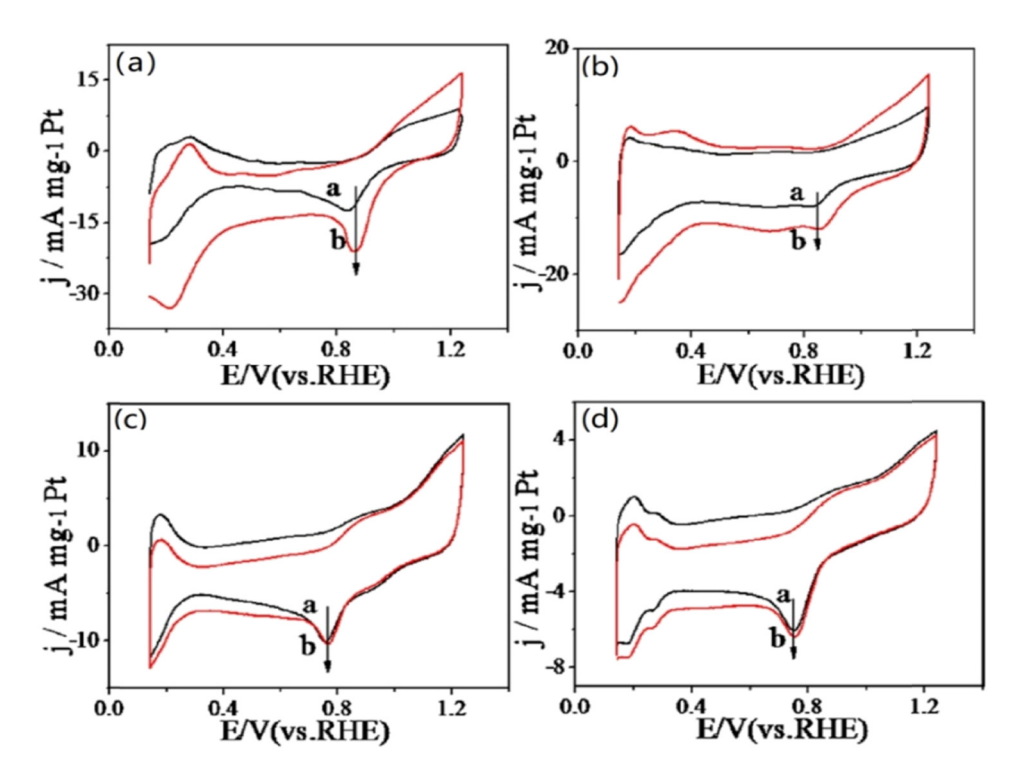


Figure 10: CV Curves in oxygen saturated H_2SO_4 without a and with b light irradiation: (a) Pt-WO₃@W/GNs, (b) Pt/WO₃-GN, (c) 30% PtRu-C, (d) Pt/GNs [110].

 Fable 5: Examples of applications of CV or LSV

Catalyst	Synthesis method	Current density	Max current density Catalytic activity	Catalytic activity	Ref.
γ-Al ₂ O3 CuO/α-Fe ₂ O ₃ /γ-Al ₂ O ₃	Wet chemical method	$y-Al_2O_3 < CuO/\alpha - Fe_2O_3/y-Al_2O_3$	69 µA·mg ^{−1}	$y-Al_2O_3 < CuO/\alpha-Fe_2O_3/y-Al_2O_3$	[111]
g-C ₃ N ₄ g-C ₃ N ₄ -La ₂ O ₃ g-C ₃ N ₄ -CoO g-C ₃ N ₄ - Hydrothermally prepared		$g-C_3N_4 < g-C_3N_4-La_2O_3 < g-C_3N_4-CoO$	3.75 mA·mg ^{−1}	$g-C_3N_4 < g-C_3N_4$ - $La_2O_3 < g-C_3N_4$ -CoO < g - [112]	[112]
La ₂ O ₃ -CoO		< g-C ₃ N ₄ -La ₂ O ₃ -CoO		C ₃ N ₄ -La ₂ O ₃ -CoO	
ZW_4	Facile	$ZW_4 <$	70	ZW ₄ <	[113]
5GZW ₄ -I	Coprecipitating	5GZW ₄ -I	µA∙mg ^{−1}	5GZW ₄ -I	
10GZW ₄ -I	Method	< 10GZW ₄ -I		< 10GZW ₄ -I	

the peak current of Pt-WO₃@W/GNs was the highest in the presence of light radiation, which was 1.7 times higher than that without light. As shown in Figure 10(b), the mass activity of Pt/WO₃-GNs also increased under light irradiation, but the increased amplitude was obviously smaller than that of Pt-WO₃@W/GNs. On the contrary, the current density of 30% PtRu-C and Pt/GNs in Figure 10(c) and (d) increased negligibly under light irradiation, which might be due to the lack of light-responsive W species. Notably, the mass activity (peak current density) of Pt-WO₃@W/GNs for ORR was the highest under light illumination, with a digital of 21.34 mA·mg⁻¹. Hence, Pt-WO₃@W/GNs exhibited the most photocatalytic advantages compared with the other three catalysts for ORR. All in all, it could be inferred Pt-WO₃@W/GNs gave higher photoelectrocatalytic performance in ORR.

So as to better understand the application of CV or LSV in photocatalysis, several examples in the past 3 years (as shown in Table 5) are added to further illustrate. Generally speaking, CV or LSV can compare the current density of photocatalysts to judge the catalytic activity.

2.8 Chronoamperometry (photocurrent)

Photocurrent is a simple and extensively used photoelectrochemical detection technology [114,115]. When light energy is used to excite a semiconductor, VB electrons are excited and transit to the CB. By adding a strong electric field, the CB electrons will move directionally and form a current. Photogenerated current potentiated is used in electrolytic cells to reduce some electroactive substances in solution. The current time curve, namely photocurrent spectrum, is obtained by recording the change of current with time [116,117].

Photocurrent is an electrochemical analysis method and technology for studying the kinetics of electrochemical processes. It represents a functional relationship, which is a change in current over time after applying a single or double potential to the working electrode of a photochemical system [118,119]. The research on the principle of the photocurrent method can be traced back to 1902 when the Cottrell equation appeared. Cottrell equation was mathematically derived from the diffusion law of linear diffusion on a planar electrode and Laplace transform [120]. There is a quantitative relationship between the parameters (Eq. 16).

$$i_1 = \frac{nFAD^{\frac{1}{2}}C_0}{\left[\pi t^{\frac{1}{2}}\right]} \tag{16}$$

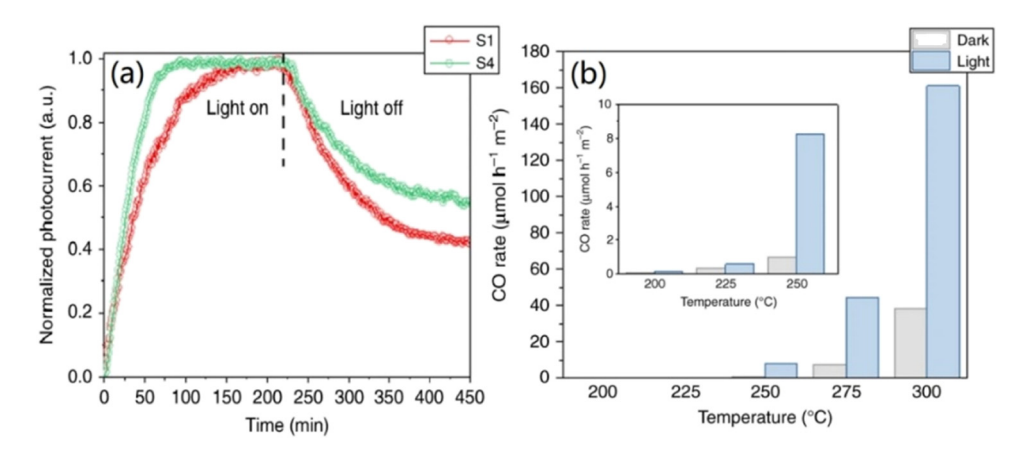


Figure 11: (a) Photocurrent saturation and decay plot acquired at $\sim 200^{\circ}$ C with a 1:1 ratio of CO_2/H_2 and under a 100 W LED white lamp. (b) Catalytic performance of S4 in photocatalytic CO_2 hydrogenation reaction at different temperatures [128].

Table 6: Examples of applications of photocurrent

Catalyst	Synthesis method	Photocurrent response	Charge separation ability	Ref.
CdS 6% MoS ₂ /CdS ZnWO ₄ 5GZW ₄ -I	Sonication method Coprecipitating method	CdS < 6% MoS ₂ /CdS ZW ₄ < 5GZW ₄ -I <	CdS < 6% MoS ₂ /CdS ZW ₄ < 5GZW ₄ -I <	[98] [113]
10GZW ₄ -I 15GZW ₄ -I		15GZW ₄ -I < 10GZW ₄ -I	15GZW ₄ -I < 10GZW ₄ -I	
Cu ₂ O Cu ₂ O-MoS ₂ Cu ₂ O-MoS ₂ /rGO	Hydrothermal route	Cu ₂ O < Cu ₂ O-MoS ₂ < Cu ₂ O-MoS ₂ /rGO	Cu ₂ O < Cu ₂ O-MoS ₂ < Cu ₂ O-MoS ₂ /rGO	[129]

where i_1 is the limiting current, n is the quantity of electron transfer in the electrode reaction, A is the electrode area, F is the Faraday constant, D is the diffusion coefficient of the active substance, C_0 is the initial molar concentration of the active substance in the solution, and t is the electrolytic time.

The concentration of the active substance on the electrode surface will decrease gradually due to electrolysis, so the current will decrease correspondingly as time increases, which is reflected in the Cottrell equation. In addition, i_1 is proportional to C_0 [121–123].

Photocurrent is an efficient characterization technique with high sensitivity and less detection time for the analysis and understanding of photodynamics occurring in semiconductors [124,125]. Traditional photocurrent can explore the morphology, material properties, and contact interface of semiconductor catalytic materials [126]. At present, it is considered one of the effective methods to determine the separation capacity of photo-borne carriers. When the photocurrent energy is absorbed by the semiconductor, the higher photocurrent response indicates a better charge separation ability [127].

Wang's work gives a classic example of the characterization of optical properties of photocatalysts via photocurrent [128]. The non-stoichiometric degree of In₂O₃ was controlled by them to adjust the color of the catalyst and make its color turn from light yellow to black. Photocatalysts S1 and S4 (S1 was In₂O₃ nanocrystals, which was obtained by thermally dehydroxylating In(OH)₃ nanocrystals in air at 700°C for 5 h. S4 was produced by placing the as prepared S1 with hydrogen at 400°C for 1h, to form In₂O_{3-x}/In₂O₃) were prepared. The photocurrent responses of S1 and S4 catalysts were characterized. As can be seen from Figure 11(a), under the condition of light illumination, compared with S1, S4 excited electrons within a shorter saturation time, indicating that S4 was strong in light absorption. Under the cases of light-off, the photocurrents of S1 and S4 decayed gradually. S4 took more decay time than S1, probably due to the more oxygen vacancy traps and longer photoelectron lifetimes. The increase of oxygen vacancies in S4 was beneficial to increase the lifetime of photoelectrons and consequently boosted the catalytic performance. In other words, the higher photocurrent response mentioned above indicated

Table 7: Brief summary of techniques for the characterization of optical properties of photocatalysts

Techniques	Principles	Main information obtained	Advantages	Disadvantages
UV-vis absorption spectroscopy	Electronic transition	Light absorption capacity and band gap	Simple operation, fast analysis speed, and high accuracy	High concentrations are not applicable, and high cost
UV-vis diffuse reflection spectroscopy (UV-vis DRS)	Electronic transition	Light reflection capacity	Simple operation, fast analysis speed, and high accuracy	High cost
PL 1	Electronic transition	Electron hole recombination rate	Simple operation, and high resolution,	High requirements for temperature, and it can't be used for quantitative analysis
Raman spectroscopy	Light scattering	Vibrational or rotational energy level of molecules	Simple operation, and high sensitivity	Nonlinearity of curve
Mott–Schottky plot	Mott–Schottky equation	The position of the flat band potential	Simple operation	Data processing is complex
EIS	The change of impedance with frequency	Charge transfer capacity	Simple operation and high accuracy	Simple operation and high accuracy There is no unique correspondence between impedance spectrum and equivalent circuit
rsv	Current varies with voltage	The position of the effective potential	Simple operation, low detection cost and fast test process	Poor stability
Λ	Current varies with voltage	Current density generated by photocatalysts	Simple operation	Unable to analyze from dynamics
Chronoamperometry (photocurrent)	Change in current over time	Evaluate the separation ability of photogenerated electron-hole pairs	Simple detection and high sensitivity	Data processing is complex

better charge separation ability. In Figure 11(a), we can see that the photocurrent response of S4 was higher than that of S1, which indicates that the charge separation ability of S4 was higher than that of S1. Apparently, in Figure 11(b), S4 recorded a better catalytic performance in photocatalytic $\rm CO_2$ hydrogenation reaction, with a CO productivity of 160.99 μ mol·h⁻¹·m⁻².

For photocurrent as a characterization technique, several examples from the last 3 years are added in Table 6. The ability of charge separation was evaluated by photocurrent response.

3 Conclusions and outlooks

Photocatalysis is a research hotspot for both energy and environment. As effective tools for the characterization of photocatalysts, the related techniques are becoming increasingly necessary.

Catalysts for photocatalysis are mainly consist of semiconductor materials, and characterization techniques for photocatalysts are also of significance. (Main point characterization techniques are shown in Table 7.) According to the information (such as the energy band positions, the light absorption ability, and the recombination ability of photogenerated electron—hole pairs) obtained from several tests, researchers could obtain theoretical support to understand the properties of semiconductor photocatalysts comprehensively.

Nowadays, there are more and more advanced characterization techniques for semiconductor photocatalysts; however, these techniques still have some practical deficiencies including sensitivity, resolution, and skills for insitu tests. Therefore, researchers should not only be fully familiar with the working principles of existing characterization techniques but also optimize the richness and relevance of device applications, which is conducive to making clear the photocatalytic reaction mechanism. In addition, although the present CV can analyze the activity of redox reactions in photocatalysis from the perspective of thermodynamics (Gibbs free energy and entropy increase principle), it is still incapable of studying the reaction process through kinetics. Therefore, the development of a new method that can be analyzed from the perspective of thermodynamics as well as the view of dynamics and will play a key part in promoting the development of photocatalysis.

Acknowledgements: We acknowledge the financial support from the National Natural Science Foundation of America China (No. 21902116), Scientific Research Foundation

of Liaoning Province (2022JH2/101300125), and the Education Department of Liaoning Province (JQL202015401 and LJKMZ20220982).

Funding information: Authors state no funding is involved.

Author contributions: Chunnan Hao: writing – original draft, writing – review & editing; Zenan Ni: funding acquisition, writing – original draft; Jian Wang: writing – review & editing; Huimin Liu: funding acquisition, writing – review & editing; Ze Zheng: formal analysis; Yuqiao Li: formal analysis; Jiawen Guo: formal analysis; Ruiqi Zhang: formal analysis; Qijian Zhang: conceptualization, supervision, funding acquisition, writing – review & editing.

Conflict of interest: Authors state no conflict of interest.

References

- Lu Y, Zhang H, Fan D, Chen Z, Yang X. Coupling solar-driven photothermal effect into photocatalysis for sustainable water treatment. J Hazard Mater. 2022;423:127–8.
- [2] Sagir M, Tahir MB, Waheed U. Akram J in Role of Photocatalysis in Green Energy Production. Oxford: Elsevier; 2022. p. 590–6.
- [3] Wu J, Zheng W, Chen Y. Definition of photocatalysis: current understanding and perspectives. Curr Opin Green Sustainable Chem. 2022;33:100580-5.
- [4] Xing X, Tang S, Hong H, Jin H. Concentrated solar photocatalysis for hydrogen generation from water by titaniacontaining gold nanoparticles. Int J Hydrogrn Energ. 2020;45(16):9612–23.
- [5] Prasannalakshmi P, Shanmugam N. Fabrication of TiO₂/ZnO nanocomposites for solar energy driven photocatalysis. Mat Sci Semicon Proc. 2017;61:114–24.
- [6] Fujishima A, Honda K. Electrochemical photolysis of water at a semiconductor electrode. Nature. 1972;238(5358):37–8.
- [7] Fujishima A, Sugiyama E, Honda K. Photosensitized electrolytic oxidation of iodide ions on cadmium sulfide single crystal electrode. Bull Chem Soc Jpn. 2006;44(1):304.
- [8] Calzaferri PG, Forss L, Spahni W. Photovoltaische umwandlung und speicherung der sonnenenergie. Chem Unserer Zeit. 1987;21(5):161–74.
- [9] Yi M, Wang X, Jia Y, Chen X, Li C. Titanium dioxide-based nanomaterials for photocatalytic fuel generations. Chem Rev. 2014;114(19):9987–10043.
- [10] Wang Z, Song H, Liu H, Ye J. Coupling of solar energy and thermal energy for carbon dioxide reduction: status and prospects. Angew Chen Int Edit. 2020;59(21):8016–35.
- [11] Schneider J, Matsuoka M, Takeuchi M, Zhang J, Horiuchi Y, Anpo M, et al. Understanding TiO₂ photocatalysis: mechanisms and materials. Chem Rev. 2014;114(19):9919–86.
- [12] Zhou WC, Zhang WD. Anchoring nickel complex to g-C₃N₄ enables an efficient photocatalytic hydrogen evolution reaction through ligand-to-metal charge transfer mechanism. J Colloid Interf Sci. 2022;616:791–802.

- [13] Shyamala R, Devi LG. Reduced graphene oxide/SnO₂ nanocomposites for the photocatalytic degradation of rhodamine B: preparation, characterization, photosensitization, vectorial charge transfer mechanism and identification of reaction intermediates. Chem Phys Lett. 2020;748:137385-96.
- Laohhasurayotin K, Pookboonmee S. Multifunctional properties of Aq/TiO₂/bamboo charcoal composites: Preparation and examination through several characterization methods. Appl Surf Sci. 2013;282(11):236-44.
- [15] Huang S, Si Z, Weng D. The synthesis, activity, stability and the charge transfer identification of Aq:AqBr/y-Al₂O₃ photocatalyst for organic pollutant decomposition in water. Appl Surf Sci. 2015;357:1792-800.
- Yang L. Si Z. Weng D. Yao Y. Synthesis, characterization and photocatalytic activity of porous WO₃/TiO₂ hollow microspheres. Appl Surf Sci. 2014;313:470-8.
- [17] Fan W, Hu J, Jing H, Xin W, Qiu X. Electronic structure and photocatalytic activities of (Bi_{2-δ}Y_δ)Sn₂O₇ solid solution. Appl Surf Sci. 2015;357:2364-71.
- [18] Chen LC, Tu YJ, Wang YS, Kan RS, Huang CM. Characterization and photoreactivity of N-, S-, and C-doped ZnO under UV and visible light illumination. J Photoch Photobio A. 2008;199(2-3):170-8.
- [19] Niño-Martínez N, Martínez-Castañón GA, Aragón-Piña A, Martínez-Gutierrez F, Martínez-Mendoza JR, Ruiz F. Characterization of silver nanoparticles synthesized on titanium dioxide fine particles. Nanotechnology. 2008;19(6):065711-9.
- [20] Garrett DeYoung H. UV/VIS Spectroscopy: Something old, something new. Bio-Technol. 1987;5(10):1088-9.
- [21] Schramm H. UV-Vis vapor absorption spectrum of antimony(iii) chloride, antimony(v) chloride, and antimony(iii) bromide. the vapor pressure of antimony(iii) bromide. J Chem Eng. 1995;40(4):963-7.
- [22] Xw A, Yz B, Kw A, Shuai ZA, Xq A, Liang SA, et al. In-situ construction of Bi/defective Bi₄NbO₈Cl for non-noble metal based Mott-Schottky photocatalysts towards organic pollutants removal. J Hazard Mater. 2020;393(5):122408-16.
- Polignano ML, Caricato AP, Modelli A, Zonca R. Surface characterization by photocurrent measurements. Appl Surf Sci. 2000:154:276-82.
- Zhang J, Huang Q, Wang J, Zhang J, Zhao Y. Supported dual-atom [24] catalysts: Preparation, characterization, and potential applications. Chinese J Catal. 2020;41(5):783-98.
- Ali I, AlGhamdi K, Al-Wadaani FT. Advances in iridium nano catalyst preparation, characterization and applications. J Mol Liq. 2019;280:274-84.
- [26] Luo C, Ren X, Dai Z, Zhang Y, Qi X, Pan C. Present perspectives of advanced characterization techniques in TiO2-based photocatalysts. ACS Appl Mater Inter. 2017;9(28):23265-86.
- Janáky C, Rajeshwar K. Current trends in semiconductor photoelectrochemistry. ACS Energy Lett. 2017;2(6):1425-8.
- [28] Zhang L, Ran J, Qiao S, Jaroniec M. Characterization of semiconductor photocatalysts. Chem Soc Rev. 2019;48(20):5184-206.
- Chen X, Peng X, Jiang L, Yuan X, Zhang J, Yu H. Terephthalate acid [29] decorated TiO₂ for visible light driven photocatalysis mediated via ligand-to-metal charge transfer (LMCT). Colloid Surface A. 2020;603:125188-99.
- Wang N, Tan F, Zhao Y, Tsoi CC, Fan X, Yu W, et al. Optofluidic UV-Vis spectrophotometer for online monitoring of photocatalytic reactions. Sci Rep-Uk. 2016;6(1):28928-35.

- [31] Roig B, Touraud E, Thomas O. Photochemical reaction monitoring by ultra-violet spectrophotometry. Spectrochim Acta A. 2002;58(13):2925-30.
- [32] Mustafa YF, Khalil RR, Mohammed ET, Bashir M, Oglah MK. Effects of Structural Manipulation on the Bioactivity of some Coumarin-Based Products. Arch Razi Inst. 2021;76(5):1297-305.
- Timothy N, Envelope Z. The promise and pitfalls of photocatalysis for organic synthesis. Chem Catalysis. 2022;2(3):468-76.
- [34] Jing Z, Feng C, Zhang J. Carbon-Deposited TiO₂: Synthesis, Characterization, and Visible Photocatalytic Performance. J Phys Chem C. 2010;114(2):933-9.
- Zhang X, Yuan X, Jiang L, Zhang J, Zeng G. Powerful combination of 2D g-C₃N₄ and 2D nanomaterials for photocatalysis: Recent advances. Chem Eng J. 2020;390:124475-503.
- Wang N, Zhang X, Wang Y, Yu W, Chan H. Microfluidic reactors for [36] photocatalytic water purification. Lab Chip. 2014;14:1074-82.
- [37] He X, Liu M, Liang Z, Wang Z, Wang P, Liu Y, et al. Photo-enhanced CO₂ hydrogenation by plasmonic Cu/ZnO at atmospheric pressure. J Solid State Chem. 2021;298(1):122113-20.
- Willardson P, Beer A. Physics of III-V Compounds. Semiconductors & Semimetals. Oxford: Elsevier; 1966. p. 3-472.
- [39] Li C, Zhang D, Han S, Liu X, Tang T, Zhou C. Diameter-Controlled Growth of Single-Crystalline In₂O₃ Nanowires and Their Electronic Properties. Adv Mater. 2003;15(2):143-6.
- [40] Ohhata Y, Shinoki F, Yoshida S. Optical properties of r.f. reactive sputtered tin-doped In₂O₃ films. Thin Solid Films. 1979;59(2):255-61.
- [41] Nor N, Amin N. Glucose precursor carbon-doped TiO2 heterojunctions for enhanced efficiency in photocatalytic reduction of carbon dioxide to methanol. J CO2 Util. 2019;33:372-83.
- [42] Lam S, Sin J, Abdullah A, Mohamed AR. Transition metal oxide loaded ZnO nanorods: Preparation, characterization and their UV-vis photocatalytic activities. Sep Purif Technol. 2014:132:378-87.
- [43] Hannus I, Tóth T, Méhn D, Kiricsi I. UV-vis diffuse reflectance spectroscopic study of transition-metal (V, Ti) containing catalysts. J Mol Struct. 2001;563:279-82.
- Yuan M, Zhang J, Song Y, Luo G, Qian X, Xiang W, et al. Effect of Nd₂O₃ addition on the surface phase of TiO₂ and photocatalytic activity studied by UV Raman spectroscopy. J Alloy Compd. 2011:509(21):6227-35.
- Li H, Gao Y, Xiong Z, Liao C, Shih K. Enhanced selective photo-[45] catalytic reduction of CO₂ to CH₄ over plasmonic Au modified g-C₃N₄ photocatalyst under UV-vis light irradiation. Appl Surf Sci. 2018;439:552-9.
- [46] Morawski AW, Kusiak N, Wanaq A, Narkiewicz U, Edelmannová M, Reli M, et al. Influence of the calcination of TiO₂-reduced graphite hybrid for the photocatalytic reduction of carbon dioxide. Catal Today. 2021;380:32-40.
- Christy AA, Ozaki Y, Gregoriou VG. Modern Fourier transform infrared spectroscopy. Comprehensive Analytical Chemistry. New York, Amsterdam: Elsevier; 2011.
- [48] Hanssen LM, Kaplan S. Infrared diffuse reflectance instrumentation and standards at NIST. Anal Chim Acta. 1999;380:289-302.
- [49] Griffiths PR, Yeboah SA, Hamadeh IM, Duff PJ, Yang W, Van K. Analytical applications of diffuse reflectance infrared fourier transform spectroscopy. In: Recent Advances in Analytical Spectroscopy. New York: Pergamon Press; 1982.
- [50] Höpe A. In: Chapter 6 - Diffuse Reflectance and Transmittance. New York: Academic Press; 2014.

- [51] Krivácsy Z, Hlavay J. Determination of quartz in dust samples by diffuse reflection FTIR spectroscopy. J Mol Struct. 1993;294:251–4.
- [52] Shen J, Li Y, He J. On the Kubelka–Munk absorption coefficient. Dyes Pigments. 2016;127:187–8.
- [53] Christy AA, Kvalheim OM, Velapoldi RA. Quantitative analysis in diffuse reflectance spectrometry: A modified Kubelka-Munk equation. Vib Spectrosc. 1995;9(1):19–27.
- [54] Pascariu P, Cojocaru C, Samoila P, Airinei A, Olaru N, Rotaru A, et al. Cu/TiO₂ composite nanofibers with improved photocatalytic performance under UV and UV-visible light irradiation. Surfaces and Interfaces. 2022;28:101644–58.
- [55] Singhal N, Selvaraj S, Sivalingam Y, Venugopal G. Study of photocatalytic degradation efficiency of rGO/ZnO nano-photocatalyst and their performance analysis using scanning Kelvin probe. J Environ Chem Eng. 2022;10(2):107293–304.
- [56] Karuppasamy P, Nisha N, Pugazhendhi A, Kandasamy S, Pitchaimuthu S. An investigation of transition metal doped TiO₂ photocatalysts for the enhanced photocatalytic decoloration of methylene blue dye under visible light irradiation. J Environ Chem Eng. 2021;9(4):105254–62.
- [57] Paul A, Dhar SS. Construction of hierarchical $MnMoO_4/NiFe_2O_4$ nanocomposite: Highly efficient visible light driven photocatalyst in the degradation of different polluting dyes in aqueous medium. Colloid Surface A. 2020;585:124090–9.
- [58] Sanguinetti S, Guzzi M, Gurioli M. In: 6 Accessing structural and electronic properties of semiconductor nanostructures via photoluminescence. New York: Academic Press; 2008.
- [59] Anpo M, Che M. Applications of photoluminescence techniques to the characterization of solid surfaces in relation to adsorption, catalysis, and photocatalysis. Adv Catal. 1999;44(2):119–257.
- [60] Stevanovic A, Buettner M, Zhang Z, Yates J. Photoluminescence of TiO₂: Effect of UV light and adsorbed molecules on surface band structure. J Am Chem Soc. 2012;134(1):324–32.
- [61] Santos N, Rodrigues J, Pereira S, Fernandes A, Monteiro T, Costa F. Electrochemical and photoluminescence response of laserinduced graphene/electrodeposited ZnO composites. Sci Rep. 2021;11:17154–68.
- [62] Kumari S, Gusain R, Kumar A, Manwar N, Khatri OP. Direct growth of nanostructural MoS₂ over the h-BN nanoplatelets: An efficient heterostructure for visible light photoreduction of CO₂ to methanol. J CO2 Util. 2020;42:101345–55.
- [63] Chang CJ, Teng MC, Chen J, Lin YG, Chen CY. Microwave solvothermal synthesis of cubic MnS@Ag₂S core-shell photocatalysts with improved charge separation and photocatalytic activity. Appl Surf Sci. 2021;558:149875–84.
- [64] Cen S, Lv X, Liu Q, Li D, Jiang Y, Hou C, et al. Direct Z-scheme Ag₂WO₄/BiOCl composite photocatalyst for efficient photocatalytic degradations of dissolved organic impurities. Optik. 2021;243:166847–56.
- [65] Swaminathan V, Jayaraman A. Encyclopedia of Materials: Science and Technology. 2nd edn. New York: Academic Press; 2001. p. 8387–91.
- [66] Cantarero A. Raman scattering applied to materials science. Procedia Mater Sci. 2015;9:113–22.
- [67] Du X, Liu D, An K, Jiang S, Wei Z, Wang S, et al. Advances in oxide semiconductors for surface enhanced Raman scattering. Appl Mater Today. 2022;29:101563.
- [68] Larkin PJ. Infrared and Raman Spectroscopy. Oxford: Academic Press; 2018. p. 1–5.

- [69] Marzi J, Brauchle E, Carvajal Berrio DA, Lee Layland S, Schenke K. 3.7 Raman Spectroscopy. Oxford: Academic Press; 2017. p. 108–27.
- [70] Akshhayya C, Okla MK, Al-ghamdi AA, Abdel-Maksoud MA, AbdElgawad H, Das A, et al. Construction of S-scheme heterojunction CuFe₂O₄/α-MnO₂ with tuned bandgap for enhanced white light harvesting: Insights of photoluminescence, Raman scattering and photocatalysis. Surfaces and Interfaces. 2021:27:101523.
- [71] Ribeiro-Claro P, Nolasco MM, Araújo C. Chapter 5 Characterization of Microplastics by Raman Spectroscopy. Oxford: Academic Press; 2017. p. 119–51.
- [72] Hurai V, Huraiová M, Slobodník M, Thomas R. Chapter 7 Raman and Infrared Spectroscopic Analysis. Oxford: Academic Press; 2015. p. 231–79.
- [73] Wolverson D. Chapter 17 Raman Spectroscopy. Oxford: Academic Press; 2013. p. 753–802.
- [74] Zhang M, Zhao S, Lu Q. Enhanced photocatalytic performance of silver-based solid solution heterojunctions prepared by hydrothermal method. Mat Sci Semicon Proc. 2018;85:52–8.
- [75] Tristao JC, Magalhaes F, Corio P, Sansiviero MT. Electronic characterization and photocatalytic properties of CdS/TiO₂ semiconductor composite. J Photoch Photobio A. 2006;181:152–7.
- [76] Hamad H, Elsenety MM, Sadik W, El-Demerdash A, Nashed A, Mostafa A, et al. The superior photocatalytic performance and DFT insights of S-scheme CuO@TiO₂ heterojunction composites for simultaneous degradation of organics. Sci Rep. 2022;12(1):2217–36.
- [77] Dutta K, Sherley Saraffin R, Dutta B, Datta A, Kapuria A, Ghosh S, et al. Room temperature synthesis of GO/Ag₂O nanocomposite: Broad spectral ranged solar photocatalyst and high efficacy antibiotic for waste water treatment. J Environ Chem Eng. 2022;10(2):107175–86.
- [78] Hossain SS, Tarek M, Munusamy TD, Karim KM, Khan M. Facile synthesis of CuO/CdS heterostructure photocatalyst for the effective degradation of dye under visible light. Environ Res. 2020;188:109803–12.
- [79] Grätzel M. Photoelectrochemical cells. Nature. 2001;414(6861):338–44.
- [80] Xiong D, Zhang Q, Verma SK, Bao XQ, Li H, Zhao X. Crystal structural, optical properties and mott-schottky plots of p-type Ca doped CuFeO₂ nanoplates. Mater Res Bull. 2016;83:141–7.
- [81] Gelderman K, Lee L, Donne SW. Flat-Band Potential of a Semiconductor: Using the Mott-Schottky Equation. J Chem Educ. 2007;84(4):685–8.
- [82] Adán M, Silva T, Demourgues G, Montemor M. Application of the Mott-Schottky model to select potentials for EIS studies on electrodes for electrochemical charge storage. Electrochim Acta. 2018;289(1):47–55.
- [83] Liu D, Feng L, Cao L, Xiao T, Huang J. W/O site replace by Ce/N of Bi_2WO_6 as cations/anions to regulate the reduction potential of conduction band for enhanced photocatalytic degradation and hydrogen evolution capacity. J Alloy Ccompd. 2022;890:161920–33.
- [84] Cao J, Kako T, Peng L, Ouyang S, Ye J. Fabrication of p-type CaFe₂O₄ nanofilms for photoelectrochemical hydrogen generation. Electrochem Commun. 2011;13(3):275–8.
- [85] Cardoso J, Stulp S, Brito J, Flor J, Frem J, Zanoni M. MOFs based on ZIF-8 deposited on TiO₂ nanotubes increase the surface

- adsorption of CO2 and its photoelectrocatalytic reduction to alcohols in aqueous media. Appl Catal B:Environ. 2018;225(5):563-73.
- Preethi LK, Antony RP, Mathews T, Walczak L, Gopinath CS. A Study on Doped Heterojunctions in TiO₂ Nanotubes: An Efficient Photocatalyst for Solar Water Splitting. Sci Rep. 2017;7(1):14314-28.
- [87] Yadav R, Verma V, Mishra A, Pal N, Khan A, Sinha AK. Si incorporated Pt nanoparticles on TixSi_{1-x}O₂ support: Photo-thermal CO₂ reduction-ScienceDirect. J CO₂ Util. 2021;47:101502-12.
- Zhu L, Li H, Xia P, Liu Z, Xiong D. Hierarchical ZnO Decorated with CeO₂ Nanoparticles as the Direct Z-Scheme Heterojunction for Enhanced Photocatalytic Activity. ACS Appl Mater Inter. 2018:10(46):39679-87.
- [89] Ângelo J, Magalhães P, Andrade L, Mendes A. Characterization of TiO₂-based semiconductors for photocatalysis by electrochemical impedance spectroscopy. Appl Surf Sci. 2016;387:183-9.
- [90] Jabbar Z, Graimed B, Okab A, Issa M, Ammar S, Khadim H, et al. A review study summarizes the main characterization techniques of nano-composite photocatalysts and their applications in photodegradation of organic pollutants. Environ Nanotechnolo, Monit Manage. 2023;19:100765-84.
- [91] Wang S, Zhang J, Gharbi O, Vivier V, Gao M, Orazem ME. Electrochemical impedance spectroscopy. Nat Rev Methods Primers. 2021;1(1):41-97.
- Rooij M. Electrochemical Methods: Fundamentals and [92] Applications. Anti-Corrosion Method M. 2003;50(5):A25.
- [93] Magar HS, Hassan RY, Mulchandani A. Electrochemical Impedance Spectroscopy (EIS): Principles, construction, and biosensing applications. Sensors. 2021;21(19):6578-98.
- [94] Park SM, Yoo JS. Electrochemical impedance spectroscopy for better electrochemical measurements. Anal Chem. 2003;75(21):455A-61A.
- [95] Hauff EV. Impedance spectroscopy for emerging photovoltaics. J Phys Chem C. 2019;123(18):11329-46.
- [96] Wu Q, Li Z, Zhang X, Xu C, Ni M, Cen K, et al. Oxygen-vacancyanchoring NixOy loading towards efficient hydrogen evolution via photo-thermal coupling reaction. J Energy Chem. 2021;61:77-87.
- [97] Yu H, Han Q. Effect of reaction mediums on photocatalytic performance of BiOX (X = Cl, Br, I). Opt Mater. 2021;119:111399-410.
- Zhao H, Fu H, Yang X, Xiong S, Han D, An X. MoS₂/CdS rod-like [98] nanocomposites as high-performance visible light photocatalyst for water splitting photocatalytic hydrogen production. Int J Hydrogen Energ. 2022;47(13):8247-60.
- Wang J, Zeng H. Recent advances in electrochemical techniques for characterizing surface properties of minerals. Adv Colloid. Interface. 2021;288:102346-66.
- [100] Surendra BS. Green engineered synthesis of Ag-doped CuFe₂O₄: Characterization, Cyclic Voltammetry and Photocatalytic studies. J Sci Adv Mater Devices. 2018;3(1):44-50.
- Ming H, Zhang H, Ma Z, Huang H, Lian S, Wei Y, et al. Scanning transmission X-ray microscopy, X-ray photoelectron spectroscopy, and cyclic voltammetry study on the enhanced visible photocatalytic mechanism of carbon– ${\rm TiO_2}$ nanohybrids. Appl Surf Sci. 2012;258(8):3846-53.
- [102] Pletcher D, Greff R, Peat R, Peter LM, Robinson J. Instrumental Methods in Electrochemistry. United Kingdom: Woodhead Publishing; 2010. p. 178-228.
- [103] Zeng Y, Lu D, Kondamareddy KK, Wang H, Wu Q, Fan H, et al. Enhanced visible light photocatalysis and mechanism insight for

- novel Z-scheme MoS₂/Aq₂S/AqVOx ternary heterostructure with fast interfacial charges transfer. J Alloy Ccompd. 2022;908:164642-55.
- [104] Zaman MB, Mir RA, Poolla R. Growth and properties of solvothermally derived highly crystalline Cu₂ZnSnS₄ nanoparticles for photocatalytic and electrocatalytic applications. Int J Hydrogrn Energ. 2019;44(41):23023-33.
- [105] Bhuvanendran N, Ravichandran S, Xu Q, Maiyalagan T, Su H. A quick guide to the assessment of key electrochemical performance indicators for the oxygen reduction reaction: A comprehensive review. Int J Hydrogrn Energ. 2022;47(11):7113-38.
- [106] Prasad MA, Sangaranarayanan MV. Analysis of the diffusion layer thickness, equivalent circuit and conductance behaviour for reversible electron transfer processes in linear sweep voltammetry. Electrochimica Acta. 2004;49(3):445-53.
- [107] Yi J, Xu R, Wu Q, Zhang T, Zang K, Luo J, et al. Atomically Dispersed Iron-Nitrogen Active Sites within Porphyrinic Triazine-based Frameworks for Oxygen Reduction Reaction in Both Alkaline and Acidic Media. ACS Energy Lett. 2018;3(4):883-9.
- [108] Shan A, Huang S, Zhao H, Jiang W, Lau WM. Atomic-scaled surface engineering Ni-Pt nanoalloys towards enhanced catalytic efficiency for methanol oxidation reaction. Nano Res. 2020:13(11):1-10.
- [109] Yin S, Xu Y, Liu S, Yu H, Wang Z, Li X, et al. Binary nonmetal S and P-co-doping into mesoporous PtPd nanocages boosts oxygen reduction electrocatalysis. Nanoscale. 2020;12(27):14863-9.
- [110] Li Z, Xu S, Shi Y, Zou X, Lin S. Metal-Semiconductor Oxide (WO₃@W) induces an efficient electro-photo synergistic catalysis for MOR and ORR. Chem Eng J. 2021;414:128814-24.
- [111] Kanwal A, Sajjad S, Leghari S, Yousaf Z. Cascade electron transfer in ternary CuO/α-Fe₂O₃/γ-Al₂O₃ nanocomposite as an effective visible photocatalyst. J Phys Chem Solids. 2021;151(9):109899-912.
- [112] Iqbal N. Tailoring g-C₃N₄ with lanthanum and cobalt oxides for enhanced photoelectrochemical and photocatalytic activity. Catalysts. 2022;12(1):15-33.
- Ahmed AI, Kospa DA, Gamal S, Samra SE, Salah AA, El-Hakam SA, et al. Fast and simple fabrication of reduced graphene oxide-zinc tungstate nanocomposite with enhanced photoresponse properties as a highly efficient indirect sunlight driven photocatalyst and antibacterial agent. J Photochem Photobiol A. 2022;429:113907-18.
- [114] Wang XT, Lin XF, Yu DS. Metal-containing covalent organic framework:a new type of photo/electrocatalyst. Rare Met. 2022;41:1160-75.
- [115] Hiesgen R, Meissner D. Nanoscale photocurrent variations at metal-modified semiconductor surfaces. J Phys Chem B. 1998;102(34):6549-57.
- [116] Ma X, Mai M, Lin H, Zeng L, Zhang J, Zhou H, et al. A novel electrochemical method for simultaneous measurement of realtime potentials and photocurrent of various photoelectrochemical systems. J Power Sources. 2019;415:99-104.
- [117] Song SB, Yoon S, Kim SY, Yang S, Seo SY, Cha S, et al. Deepultraviolet electroluminescence and photocurrent generation in graphene/hBN/graphene heterostructures. Nat Commun. 2021;12:7134-42.
- [118] Zheng L, Han S, Hui L, Yu P, Fang X. Hierarchical MoS₂ Nanosheet@TiO₂ Nanotube Array Composites with Enhanced Photocatalytic and Photocurrent Performances. Small. 2016;12(11):1527-36.

- [119] Tian R, King PJ, Coelho J, Park SH, Horvath D, Nicolosi V, et al. Using chronoamperometry to rapidly measure and quantitatively analyse rate-performance in battery electrodes. J Power Sources. 2020;468:228220–30.
- [120] Jungner EW. Electrode for reversible galvanic batteries. Application granted granted Critical. 1908;14:884903.
- [121] Shi H, Li Y, Wang K, Li S, Wang X, Wang P, et al. Mass-transfer control for selective deposition of well-dispersed AuPd cocatalysts to boost photocatalytic H₂O₂ production of BiVO₄. Chem Eng J. 2022;443:136429–37.
- [122] Xiang L, Gao F, Yong Y, Wang T. A facile electrochemical approach To Form TiO₂/Ag heterostructure films with enhanced photocatalytic activity. Ind Eng Chem Res. 2015;55(1):107–15.
- [123] Oheda H. Analysis of the modulated photocurrent in amorphous semiconductors. Solid State Commun. 1980;33(2):203–6.
- [124] Xu H, Rebollar D, He H, Chong L, Liu Y, Liu C, et al. Highly selective electrocatalytic CO_2 reduction to ethanol by metallic clusters dynamically formed from atomically dispersed copper. Nat Energy. 2020;5(8):623–32.

- [125] Markovskaya DV, Zhurenok AV, Cherepanova SV, Kozlova EA. Solid solutions of CdS and ZnS: Comparing photocatalytic activity and photocurrent generation. Appl Surface Sci Adv. 2021;4:100076–83.
- [126] Cheng Y, Zhang J, Chen C, Xiong X, Zeng J, Xi J, et al. A novel 2D/2D MoSe₂/SnSe heterojunction photocatalyst with large carrier transmission channel shows excellent photoelectrochemical performance. Appl Surf Sci. 2021;563:150311–9.
- [127] Men X, Chen H, Chang K, Fang X, Wu C, Qin W, et al. Three-dimensional free-standing ZnO/graphene composite foam for photocurrent generation and photocatalytic activity. Appl Catal B-Envir. 2016;187:367–74.
- [128] Wang L, Dong Y, Yan T, Hu Z, Ali F, Meira D, et al. Black indium oxide a photothermal CO₂ hydrogenation catalyst. Nat Commun. 2020;11:2432–9.
- [129] Tiwari S, Kumar S, Ganguli AK. Role of MoS₂/rGO co-catalyst to enhance the activity and stability of Cu₂O as photocatalyst towards photoelectrochemical water splitting. J Photochem Photobiolol A. 2022;424:113622–30.